An Accessible Approach to Preparing Water-Soluble Mn^{2+}-Doped (CdSSe)ZnS (Core)Shell Nanocrystals for Ratiometric Temperature Sensing

Chih-Hao Hsia, Anna Wuttig, and Haw Yang*

Department of Chemistry, Princeton University, New Jersey 08544, United States

ABSTRACT

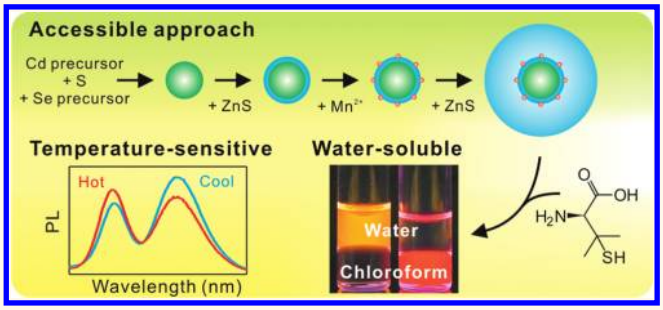

A new synthetic scheme allowing structural modifications to temperature-sensitive and water-soluble D-penicillamine-passivated Mn^{2+}-doped (CdSSe)ZnS (core)shell nanocrystals (MnQDs) was reported using air-stable chemicals. The temperature-dependent optical properties of the nanocrystals were tuned by changing their structure and composition—the ZnS shell thickness and the Mn^{2+}-dopant concentration. Thick ZnS shells significantly reduce the interference of nonradiative transitions on ratiometric emission intensities. High-dopant concentration affords consistent temperature sensitivity. In addition to the new base structure for quantum dot ratiometric temperature sensing *via* flexible, glovebox-free routes, the results also underscore the generalizability of the emission intensity ratio scheme for temperature sensing, originally proposed for rare-earth-doped materials.

KEYWORDS: nanothermometer · green chemistry · quantum dot · air stable · temperature-dependent lifetime

Temperature is a fundamental yet hitherto underappreciated thermodynamic parameter in cellular environments, affecting reaction kinetics and chemical equilibria, as well as the physical states of nucleic acids[1,2] and proteins.[3] To measure temperature in the nanoscale regime of the highly compartmentalized cellular interior, optical probes capable of remotely reporting local temperature with high spatial resolution are most desirable. Various optical probes for temperature sensing have been reported, including semiconductor quantum dots (QD),[4] fluorescent nanogels,[5] CdTe-gold nanoparticle assemblies,[6] rare-earth-doped materials,[7,8] and organic dyes.[9] For long-term temperature sensing, which is expected to be important for correlating temperature progression with cellular physiology, QD-based nanothermometers are promising because of their lasting luminescence stability.[10]

Generally, QD nanothermometers rely on the temperature-dependent changes in their excitonic emission characteristics,[4] a property that extends to the single-particle level.[11] Typically, at higher temperatures, the excitonic emission exhibits red-shifted frequency and increased nonradiative relaxation rates (shortened excited-state lifetime, also manifested as broadened emission profile and reduced intensity).[12−17] These temperature-dependent properties have been used to detect the temperature of individual living cells.[18,19] Using QDs as nanothermometers, Yang *et al.* recently reported the first experimental evidence of heterogeneous intracellular temperature progression responding to the chemical Ca^{2+} shock and the physical cold shock (rather than the commonly assumed picture that the intracellular temperature is homogeneous under all conditions).[20] The report also underscores the need for much-improved local temperature reporters because the single-parameter QD temperature sensors (based solely on the emission frequency or intensity, or the excited-state lifetime) are not sufficiently accurate for quantifying the biological and biochemical heat generation. Beyond single-parameter temperature sensing, the ratiometric scheme is expected to be more accurate because it uses two readouts to afford self-calibrated results. Recently, the ratiometric scheme has been shown to report temperature in cellular environments using

* Address correspondence to hawyang@princeton.edu.

Received for review July 9, 2011 and accepted October 28, 2011.

Published online October 28, 2011
10.1021/nn2025622

rare-earth-doped structures[21] and semiconducting polymer dots.[22] The first example of using emission intensity ratio (EIR) to sense temperature based on Boltzmann-type distribution was demonstrated in rare-earth-doped materials,[7] and subsequently studied extensively within the family of rare-earth-doped materials.[8,23] Recently, Vlaskin *et al*. extended the EIR technique to sense temperature using Mn^{2+}-doped QDs.[24] The Mn^{2+}-doped QDs have also been shown to exhibit temperature-sensing capability up to changes within 0.2 °C using the relative intensity between the excitonic and the Mn^{2+} emissions, which are both temperature dependent.[24] The salient properties of the Mn^{2+}-doped QDs make them a possible candidate for a much-improved local temperature sensor for intracellular thermometry. Until recently,[25] the temperature-sensing capability of the Mn^{2+}-doped QDs has only been demonstrated in the bioincompatible toluene solvent.

Here, we report a new approach to preparing ratiometric temperature-sensing Mn^{2+}-doped quantum dots (MnQDs) with a previously unreported base structure of (CdSSe)ZnS (core)shell where the Mn^{2+} dopant resides in the shell. Our MnQDs have completely different chemical structures but share the same temperature sensing mechanism with the one made by Vlaskin *et al*.,[24] suggesting the generalizability of the EIR temperature sensing for other materials. In addition, we demonstrated the first example of using the EIR of Mn^{2+}-doped QDs to sense temperature changes in water-based solutions.[25] The structure as well as the synthetic procedure were chosen and developed to be approachable to researchers without access to specialized synthesis instrumentation. We reasoned that the intracellular temperature variation[20] could be a very general phenomenon and a broad range of scientists, including physical biologists and biophysicists, would likely want to use intracellular temperature sensors as one of their investigative tools. Therefore, while the functionality of these new nanothermometers was our primary concern, we also pay special attention to their accessibility, that is, using air-stable chemicals and general procedures that did not require expensive and specialized equipment, such as a glovebox. The use of air-stable chemicals renders this procedure as an effort to become "greener"[26]—the cost of synthesis equipment and chemical storage and the risk associated with handling highly flammable chemicals commonly used in the synthesis of quantum dots are significantly decreased.[27] Having carefully studied the published green procedures for synthesizing MnQDs,[28,29] we were able to develop an approach that only required air-stable chemicals and standard synthesis apparatuses. We used ZnS as the chief shell composition because it allowed us to capitalize on the relatively more mature development of QD passivation with hydrophilic ligands.[30−32] Our procedure also allowed one to vary the MnQD structure at different points of the stepwise scheme to tune its temperature-sensing properties for optical readouts. To this end, we show two examples of tuning ratiometric temperature-sensing behavior by varying the thickness of the ZnS shell and the Mn^{2+} dopant concentration.

RESULTS AND DISCUSSION

To design a synthetic procedure for water-soluble ratiometric temperature-sensing MnQDs, it is important to grasp the basic physics of the sensing mechanism. The Mn^{2+}-doped QDs and the rare-earth-doped materials share a similar principle by which the temperature can be read out through the ratio of two energetically proximate emission bands.[23,24] Such an emission intensity ratio (EIR) scheme for temperature sensing has been extensively studied in rare-earth-doped materials (see ref 23 for review). Briefly, the EIR scheme utilizes the relative emission intensities from two closely separated energy levels of a single rare-earth ion dopant. When the two energy levels are thermally coupled to reach thermal equilibrium, the population of the two levels can be described by a Boltzmann-type distribution parametrized by temperature. The relative populations of the two energy levels (a function of temperature) can be approximated using the intensity ratio of the emission from the two thermally coupled levels, providing information of the surrounding temperature. To obtain reliable information from the emission intensity ratio (*e.g*., sufficient number of photons detected), the mechanism put forth by the study of rare-earth-doped materials highlights the necessity to have radiative transitions dominate over nonradiative transitions.[23] In addition, the energy separation between the two states should be small in order for efficient thermal coupling, but it should not be too small such that the two emission bands become indistinguishable. For MnQDs, it should be possible to change the temperature-sensing capacity without replacing dopants and host materials because the separation between the two emissive states can be easily tuned by varying the band gap of the semiconductor nanocrystals.[33−35]

The temperature-sensing mechanism of MnQDs can be understood by a dual emission model (*cf*. Figure 1E) as put forth by Vlaskin *et al*.,[24] analogous to the aforementioned picture for the rare-earth-doped materials. The energy separation between two emission peaks (from the excitonic states and the Mn^{2+} dopant states) in MnQDs (*cf*. Figure 1D), however, is greater than that of a typical rare-earth ion. An outline of the MnQD sensing mechanism is provided here for completeness. The energy separation in MnQDs allows a small fraction of energy in the Mn^{2+} excited states to thermally repopulate the QD's excitonic states based on the Boltzmann-type distribution. If a comparable

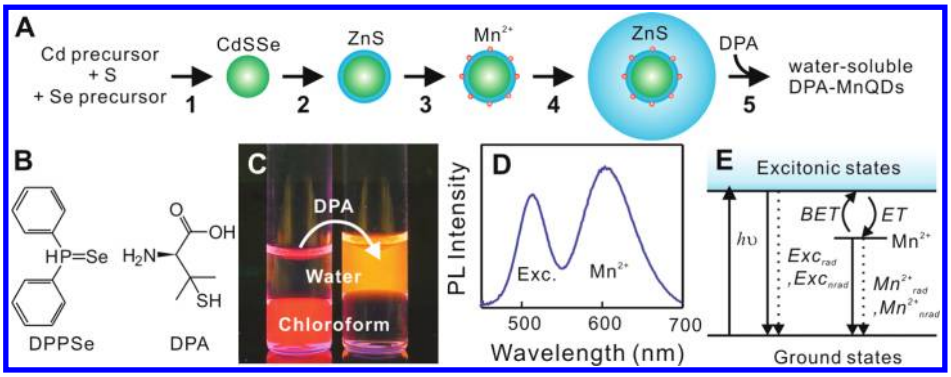

Figure 1. (A) The synthetic scheme for water-soluble Mn^{2+}-doped quantum dots coated with D-penicillamine, DPA-MnQDs. (B) The chemical structures of diphenlyphosphine selenide (DPPSe), a Se precursor for CdSSe core synthesis, and D-penicillamine (DPA). (C) A photograph of MnQDs in chloroform contrasting that of DPA-MnQDs in water. (D) A typical photoluminesecne (PL) spectrum of water-soluble DPA-MnQDs. Two emissions come from the exciton and Mn^{2+} emissions, respectively. (E) A schemetic energy diagram of MnQDs adapted from ref 24. ET and BET represent energy transfer and back energy transfer, respectively. Exc_{rad}, Exc_{nrad} represent radiative and nonradiative exciton relaxations, respectively. $Mn^{2+}{}_{rad}$, and $Mn^{2+}{}_{nrad}$ respectively represent radiative and nonradiative relaxations from Mn^{2+} excited states.

energy separation existed in rare-earth ions, temperature sensitivity would not have been observed. MnQDs, conversely, show excellent ratiometric temperature sensing behavior.[24] This result occurs because the relative lifetimes in the MnQDs between the excitonic states (10s of ns)[36−40] and the Mn^{2+}-dopant states (~2 ms)[41] are drastically different. Even though the thermally repopulated excitonic population is quite small, the significantly faster radiative decay rate of the excitonic state relative to that of the Mn^{2+}-dopant state allows for additional exciton emission signal to be observed over the lifetime of Mn^{2+} emission. This rationale implies a rapid thermal equilibrium between the excitonic and the Mn^{2+}-dopant states. Therefore, the time scale of the energy equilibration process—which includes the energy transfer (ET, from the excitonic state to the Mn^{2+} excited state) and the back energy transfer (BET, from the Mn^{2+} excited state to the excitonic state)—must be much shorter than the lifetimes of both the exciton and the Mn^{2+} emissions. Fast ET between a single pair of exciton and Mn^{2+} dopant (~60 ps, most likely dependent on the configuration details of the system) has been reported by Chen *et al.* in Mn^{2+}-doped (CdS)ZnS (core)shell nanocrystals.[42] In addition, Vlaskin *et al.*[24] have reported the time scale of ET to be shorter than 20 ps in the $(Zn_{1-x}Mn_xSe)ZnCdSe$ (core)-shell nanocrystals and suggested that the time scale for BET should also be short, although the time scale for BET was not directly measured. These prior studies[23,24] form the basis for designing the structure and composition of water-soluble temperature-sensing MnQD, described below.

We chose the (core)shell structure as the base configuration because it allows independent tuning of the composition and size of the core, the composition and thickness of the shell, and the Mn^{2+} dopant amount. In the current work, the core serves as the primary excitonic emission source, whereas the shell hosts the Mn^{2+} dopant. We chose ZnS as the host shell material to take advantage of the extensive knowledge of water-soluble ligands designed for this surface.[30−32,43−45] Here, D-penicillamine (DPA), which is inexpensive and commercially available, is used to demonstrate water solubility; nevertheless, it should be noted that other types of passivating agents are expected to work as well. DPA-coated QDs have been shown to be stable over a wide pH range and exhibit weak nonspecific binding to cells.[31] This stability has been attributed to the zwitterionic terminal of DPA and the thiol functional group surrounded by two methyl groups, which create steric constraints against oxidative dimerization of thiol ligands.[31]

With the shell material chosen, we next turned to designing a new accessible synthetic procedure that will retain the excellent temperature sensitivity of MnQDs. One of the most common core compositions for ZnS-shelled QDs is CdS. The synthetic procedure for Mn^{2+}-doped (CdS)ZnS nanocrystals reported by Yang *et al.* met the greener-approach criteria—it uses air-stable and inexpensive chemicals.[28,29] That procedure also affords the flexibility to tune the optical properties by modifying the structure of the MnQDs, for example, the radial position of Mn^{2+}-dopant and the Mn^{2+} concentration.[28] Ratiometric temperature sensing, however, was not observed in their Mn^{2+}-doped (CdS)ZnS nanocrystals (shown in Supporting Information, Figure S1). This is because the excitonic state of the (CdS)ZnS QD has a much higher energy than the excited-state of Mn^{2+} dopant such that an efficient thermal coupling between the two cannot be achieved. We reason that by doping the CdS core (bulk CdS band gap ≈ 2.42 eV) with CdSe (bulk CdSe band gap ≈ 1.74 eV), yielding $CdS_{1-x}Se_x$ core composition, the excitonic emission can be brought closer to the Mn^{2+} excited state to allow efficient coupling (shown in Supporting Information, Figure S2); hereafter the simplified designation, CdSSe, is used to

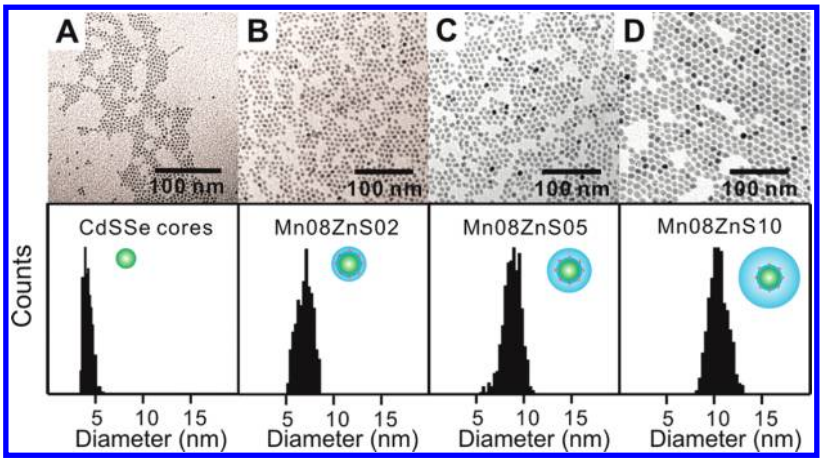

Figure 2. (A) A representative TEM image of CdSSe cores. (B–D) Representative TEM images of MnQDs with 2.4, 4.8, and 10.4 monolayers (MLs) of final ZnS shells after growth of 1.6 MLs of ZnS shells and doping of Mn cations, respectively. The average Mn^{2+} dopant per quantum dot (Mn/QD) is 8, measured by inductively coupled plasma mass spectroscopy (ICP–MS). The bottom panel shows size distribution histograms. The average diameters of CdSSe cores, Mn08ZnS02, Mn08ZnS05, and Mn08ZnS10 are 4.2, 7.0, 8.7, and 10.4 nm, respectively.

TABLE 1. Temperature Sensitivity, Precison of Temperature Sensing, Quantum Yields, and Estimated Percentages of Undoped Quantum Dots of DPA-MnQDs

sample name	temperature sensitivity[a]	precision[b]	quantum yield	undoped dots[c] (%)
DPA-Mn08ZnS02	$(2.6 \pm 0.3) \times 10^{-3}$ °C^{-1}	2.29 ± 0.42 °C	14%	7.55 ± 0.03
DPA-Mn08ZnS05	$(4.0 \pm 0.4) \times 10^{-3}$ °C^{-1}	1.61 ± 0.43 °C	11%	3.05 ± 0.06
DPA-Mn08ZnS10	$(3.0 \pm 0.3) \times 10^{-3}$ °C^{-1}	1.68 ± 0.27 °C	13%	6.8 ± 0.06
DPA-Mn02ZnS10	$(1.7 \pm 0.3) \times 10^{-3}$ °C^{-1}	2.19 ± 0.66 °C	17%	14.7 ± 0.2
DPA-Mn05ZnS10	$(3.1 \pm 0.1) \times 10^{-3}$ °C^{-1}	0.59 ± 0.20 °C	14%	14.1 ± 0.1
DPA-Mn17ZnS10	$(3.0 \pm 0.1) \times 10^{-3}$ °C^{-1}	0.79 ± 0.07 °C	8%	3.37 ± 0.07

[a] Temperature sensitivity was obtained from the slopes of temperature-dependent PL_{exc}/PL_{total} plots of DPA-MnQDs. The error bars are one standard deviation from the average values collected from the heating–cooling cycling measurements (Supporting Information, Figure S6). [b] The precision of temperature sensing (temperature-dependent uncertainty of measurement), for each sample, was the average value for uncertainties obtained at different temperatures over the heating–cooling cycles. [c] The percentages of undoped quantum dots were estimated based on the lifetime traces (see Methods section for details). The estimation assuming the ~10-ns component comes exclusively from undoped quantum dots is an upper bound for the percentage of undoped DPA-MnQDs.

indicate the core composition. We therefore designed a synthetic route based on this reasoning.

Figure 1A summarizes the synthetic scheme for temperature-sensitive DPA-coated Mn^{2+}-doped QDs (DPA-MnQDs), for which the detailed synthetic procedure and parameters are contained in the Methods section. This synthetic procedure does not require the use of the glovebox and can be carried out by simply using Schlenk lines and inexpensive, air-stable chemicals *via* Route B (the results are summarized in Supporting Information, Figure S3). In this manuscript, all of the MnQDs were made *via* Route A, where diphenylphosphine (DPP) is not air-stable; nevertheless, a glovebox is still not necessary (see Methods section for details). To further simplify the synthetic procedure, three steps (step 2–4 in Figure 1A) are combined and performed in the same flask. On the basis of the previously published reports,[28,29] the Mn^{2+} ions are likely sandwiched between the initial thin ZnS-shell coating and the thicker protective ZnS shell. The thicker external shell is one of the factors that allow retention of temperature sensitivity of this base structure in water (*vide infra*). Furthermore, synthesizing customized MnQDs for specific measurement applications is possible because this procedure permits great flexibility in tuning MnQD optical properties by varying their structure and composition. For example, the optical properties of MnQDs can be tuned by varying the size of cores and composition of shells (see Figure S4 in the Supporting Information). Here, we focus on two parameters that are expected to impact temperature sensitivity in water-soluble MnQDs using CdSSe cores—the external ZnS shell thickness and the Mn^{2+} dopant content.

For robust ratiometric temperature sensing, radiative transitions must dominate the nonradiative transitions so that sufficient number of photons can be detected. Pradhan *et al*. have reported that quenching of Mn^{2+} emission in Mn^{2+}-doped ZnSe nanocrystals was observed after ligand exchange with water-soluble thiol ligands, and the quenching of Mn^{2+} emission due to the surface trapping (one of the nonradiative

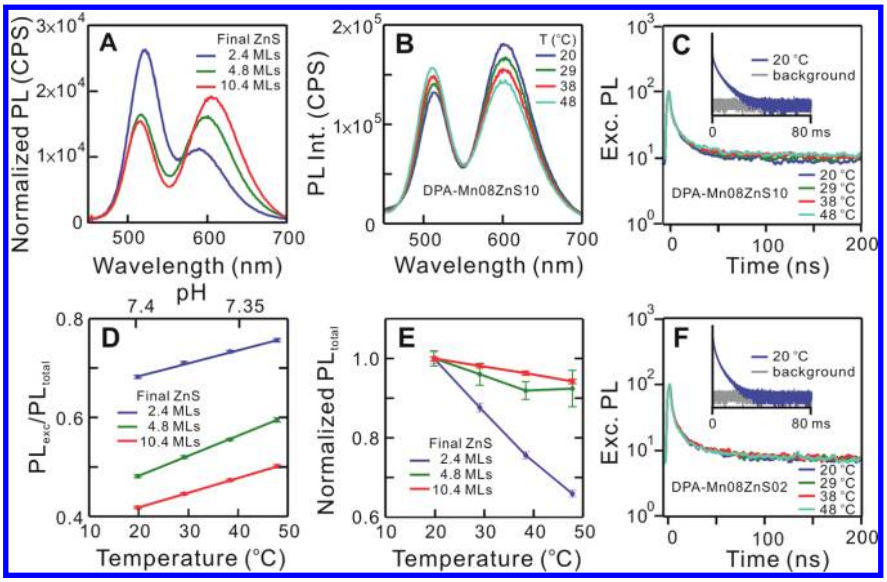

Figure 3. (A) The photoluminescence (PL) spectra of DPA-MnQDs with different ZnS shell thickness measured at 20 °C. The PL spectra were normalized to the integrated intensity. All of the data in Figure 3 was collected from DPA-MnQDs in 1X PBS buffer solution (pH = 7.4). (B) Temperature-dependent PL spectra of DPA-Mn08ZnS10. (C) Normalized temperature-dependent exciton emission lifetime traces of DPA-Mn08ZnS10. (D) Temperature-dependent exciton emission ratio (PL_{exc}/PL_{total}) plots of DPA-MnQDs with different ZnS shell thickness. The pH-value axis was measured from blank 1X PBS at different temperatures. (E) Normalized temperature-dependent total PL intensity plots of DPA-MnQDs with different ZnS shell thickness. The plots were normalized to total PL intensity at 20 °C. The error bars in panels D and E are one standard deviation from the average values collected from the heating−cooling cycling measurements (Supporting Information, Figure S6). (F) Normalized temperature-dependent exciton emission lifetime traces of DPA-Mn08ZnS02. The lifetime traces (C,F) were smoothed by averaging adjucent 17 data points and normalized to the intensity maximum. The insets in panels C and F show the exciton emission lifetime traces in millisecond time window measured at 20 °C.

pathways) can be reduced by increasing the thickness of the external ZnSe shell.[46] In addition, the fact that the exciton photoluminescence quantum yields of CdSe nanocrystals can be improved by passivating surface nonradiative recombination sites with ZnS layers has been reported in the previous studies.[47−49] Therefore, the ZnS shell thickness should play an important role for ratiometric temperature sensing in MnQDs. To examine this parameter systematically, we synthesized a series of MnQDs with different shell thicknesses. To avoid batch-to-batch variations, the samples were prepared from the same intermediate MnQDs (the intermediate MnQD structure after step 3 in Figure 1A). TEM images of the CdSSe cores and the final MnQDs show that the size of the spherical nanocrystals increases with the nominal shell thickness (Figure 2A−2D). This series of samples are called DPA-Mn08ZnS02, DPA-Mn08ZnS05, and DPA-Mn08ZnS10 for DPA-MnQDs (Mn/QD = 8) with 2.4, 4.8, and 10.4 monolayers (MLs) of external ZnS shell after the growth of nominally 1.6 MLs of ZnS shells and doping of Mn cations, respectively. The PL quantum yields of the DPA-MnQD samples reported here are tabulated in Table 1.

The photoluminescence (PL) spectra of this MnQD series are shown in Figure 3A. One can see that as the ZnS shell thickness increases, the exciton emission band (~520 nm) shifts to the blue, whereas the Mn^{2+} emission band (~600 nm) shifts to the red. The red shift of Mn^{2+} emission band is attributed to the increase in lattice pressure with increasing ZnS shell thickness.[50,51] The blue shift of exciton emission could be due to minor alloying of the nanocrystals because the final ZnS coating was performed at 280 °C, a temperature at which alloying can occur. In addition, the relative intensity of the exciton emission decreases with increasing ZnS shell thickness. This is attributed to a reduced contribution of BET with thicker ZnS shells, resulting from the increase of energy separation between the excitonic and the Mn^{2+} states. Based on a previous study,[35] alloying of (ZnSe)CdSe (core)shell nanocrystals begins at 270−280 °C, and the alloying process accelerates at temperatures higher than 290 °C. Therefore, the temperature for ZnS shell coating should not be higher than 280 °C to avoid the formation of homogenously alloyed nanocrystals, resulting in a significant decrease of exciton emission (Supporting Information, Figure S5A). To avoid alloying of the MnQDs, the ZnS shell growth was performed at a lower temperature (220 °C), and the exciton emission peaks of the MnQDs were not blue-shifted (Figure S5B), indicating no observable alloying. Unfortunately, the MnQDs using lower temperature in the ZnS shell coating did not exhibit reversible temperature sensing behavior in water-based solution (Figure S5C). Therefore, high temperature is necessary for the ZnS shell coating procedure to maintain the reversible temperature sensing (Figure S6).

TABLE 2. Nanosecond Biexponential Lifetime Fitting Results of Exciton PL Decay of DPA-MnQDs Measured at Different Temperatures

sample name	temperature (°C)	amplitude (N_{ns})	f_1[a]	τ_1 (ns)	τ_2 (ns)	offset	reduced χ^2
DPA-Mn08ZnS02	20	$(8.69 \pm 0.04) \times 10^3$	0.136 ± 0.003	0.83 ± 0.04	14.6 ± 0.1	20.6 ± 0.2	1.20
	29	$(7.40 \pm 0.03) \times 10^3$	0.134 ± 0.003	0.69 ± 0.04	13.7 ± 0.1	18.1 ± 0.2	1.22
	38	$(6.48 \pm 0.03) \times 10^3$	0.135 ± 0.003	0.69 ± 0.04	13.3 ± 0.1	16.1 ± 0.2	1.22
	48	$(5.67 \pm 0.03) \times 10^3$	0.144 ± 0.003	0.60 ± 0.04	12.3 ± 0.1	13.8 ± 0.2	1.18
DPA-Mn08ZnS05	20	$(5.81 \pm 0.03) \times 10^3$	0.153 ± 0.004	0.84 ± 0.05	10.0 ± 0.1	35.1 ± 0.2	1.07
	29	$(4.75 \pm 0.03) \times 10^3$	0.160 ± 0.005	0.70 ± 0.05	8.37 ± 0.11	30.3 ± 0.2	1.12
	38	$(4.12 \pm 0.03) \times 10^3$	0.169 ± 0.005	0.80 ± 0.05	10.3 ± 0.2	27.2 ± 0.2	1.11
	48	$(3.48 \pm 0.03) \times 10^3$	0.177 ± 0.005	0.69 ± 0.05	8.92 ± 0.14	25.4 ± 0.2	0.97
DPA-Mn08ZnS10	20	$(8.75 \pm 0.03) \times 10^3$	0.110 ± 0.003	0.67 ± 0.04	12.3 ± 0.1	23.9 ± 0.2	1.15
	29	$(8.42 \pm 0.03) \times 10^3$	0.106 ± 0.003	0.73 ± 0.05	12.9 ± 0.1	24.8 ± 0.2	1.19
	38	$(7.71 \pm 0.03) \times 10^3$	0.115 ± 0.003	0.79 ± 0.05	12.8 ± 0.1	26.2 ± 0.2	1.10
	48	$(7.46 \pm 0.04) \times 10^3$	0.122 ± 0.003	0.88 ± 0.05	14.0 ± 0.1	27.5 ± 0.2	1.16
DPA-Mn02ZnS10	20	$(7.76 \pm 0.03) \times 10^3$	0.153 ± 0.003	0.66 ± 0.04	10.5 ± 0.1	8.55 ± 0.14	1.20
	29	$(8.21 \pm 0.03) \times 10^3$	0.147 ± 0.003	0.65 ± 0.04	9.87 ± 0.06	8.66 ± 0.14	1.33
	38	$(7.37 \pm 0.03) \times 10^3$	0.150 ± 0.003	0.66 ± 0.04	9.64 ± 0.07	9.17 ± 0.14	1.15
	48	$(8.23 \pm 0.03) \times 10^3$	0.158 ± 0.003	0.80 ± 0.04	10.5 ± 0.1	9.96 ± 0.14	1.24
DPA-Mn05ZnS10	20	$(6.23 \pm 0.01) \times 10^4$	0.090 ± 0.001	2.02 ± 0.05	18.1 ± 0.1	77.7 ± 0.4	1.35
	29	$(5.65 \pm 0.01) \times 10^4$	0.093 ± 0.001	1.96 ± 0.05	18.3 ± 0.1	82.1 ± 0.4	1.22
	38	$(5.26 \pm 0.01) \times 10^4$	0.092 ± 0.001	1.91 ± 0.05	18.4 ± 0.1	88.4 ± 0.4	1.35
	48	$(4.78 \pm 0.01) \times 10^4$	0.093 ± 0.001	1.83 ± 0.05	17.4 ± 0.1	93.9 ± 0.4	1.36
DPA-Mn17ZnS10	20	$(1.89 \pm 0.02) \times 10^3$	0.272 ± 0.008	0.44 ± 0.04	5.16 ± 0.11	8.81 ± 0.13	1.17
	29	$(1.62 \pm 0.02) \times 10^3$	0.299 ± 0.008	0.49 ± 0.04	6.85 ± 0.17	9.52 ± 0.13	1.08
	38	$(1.50 \pm 0.02) \times 10^3$	0.313 ± 0.009	0.55 ± 0.04	7.10 ± 0.10	11.0 ± 0.1	1.02
	48	$(1.31 \pm 0.02) \times 10^3$	0.333 ± 0.010	0.57 ± 0.04	6.58 ± 0.22	11.7 ± 0.1	1.12

[a] f_1 is the fraction of the short lifetime (τ_1) component.

The temperature dependence of DPA-MnQD spectroscopic response with different shell thicknesses is generally similar. As a representative example, Figure 3B shows the PL spectra of DPA-Mn08ZnS10 as a function of temperature. The relative intensity of exciton emission is seen to increase with temperature. This is attributed to an increased contribution of BET at higher temperatures. The isosbestic point of these two emissions is at 565 nm, which serves as the separating wavelength for the ratiometric measurements. It is important to note that in practical applications, the ratiometric temperature sensing data can be obtained by simply using a dichroic filter set to the isosbestic point and two photodiode detectors—one for the exciton emission and one for the Mn^{2+} emission. With this measurement technique, one does not have to rely on a spectrometer and curve fitting computations, implying robust and faster measurements.

Further insights can be obtained from photoluminescence lifetime measurements. Figure 3C shows the lifetime traces of exciton emission in DPA-Mn08ZnS10 on millisecond and nanosecond time scales. The nanosecond lifetime data can be suitably modeled by two exponential decays with a constant intensity offset (see Supporting Information for visualizations of the lifetime traces and fits), and the fitting results are tabulated in Table 2 (see Method section for details). The fast decay (~1 ns) is assigned to either the exciton nonradiative relaxation and/or the energy transfer from exciton to Mn^{2+} excited states. The second, slower decay (~13 ns) is commensurate with the typical lifetime for exciton emission in quantum dots and therefore assigned to the exciton emission.[36−40] The constant plateau intensity in the lifetime trace is seen to increase with temperature. It appears flat in the 200-ns lifetime acquisition window because Mn^{2+} dopants have long-lived excited states (lifetime ≈ 2 ms)[41] and only a small fraction of energy is transferred back to the excitonic states from the Mn^{2+} excited states *via* BET. The plateau intensity shown in Figure 3C is much higher than background (see Supporting Information, Figure S9); therefore, the temperature-dependent plateau intensity is attributed to contributions from BET, originated from temperature-dependent Boltzmann-type distribution (see Table 2 for temperature-dependent plateau intensity). Indeed, the measured lifetimes of the PL decays beyond 200 ns were on the order of

TABLE 3. Millisecond Stretched Exponential Lifetime Fitting Results of Exciton PL Decay of DPA-MnQDs[a]

sample name	τ_{kww} (ms)	β	$<\tau>_{kww}$ (ms)	reduced χ^2
DPA-Mn08ZnS02	0.045	0.392	0.906	1.83
DPA-Mn08ZnS05	0.106	0.423	1.40	1.47
DPA-Mn08ZnS10	0.210	0.453	1.98	1.62
DPA-Mn02ZnS10	0.161	0.422	2.16	1.5
DPA-Mn05ZnS10	0.243	0.445	2.48	1.99
DPA-Mn17ZnS10	0.342	0.508	1.93	1.38

[a] Uncertainties were not included in this table because they are less than 0.5% of the fitted values.

TABLE 4. Millisecond Stretched Exponential Lifetime Fitting Results of Mn^{2+} PL Decay of DPA-MnQDs[a]

sample name	τ_{KWW} (ms)	β	$<\tau>_{kww}$ (ms)	reduced χ^2
DPA-Mn08ZnS02	0.324	0.482	2.28	1.24
DPA-Mn08ZnS05	0.742	0.547	3.14	1.20
DPA-Mn08ZnS10	0.971	0.564	3.68	1.42
DPA-Mn02ZnS10	1.74	0.609	5.13	1.15
DPA-Mn05ZnS10	1.66	0.595	5.25	1.69
DPA-Mn17ZnS10	0.563	0.531	2.67	2.71

[a] Uncertainties were not included in this table because they are less than 0.5% of the fitted values.

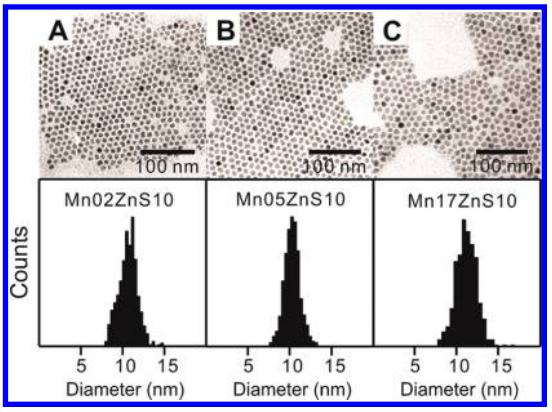

Figure 4. Representative TEM images of Mn02ZnS10 (A), Mn05ZnS10 (B), and Mn17ZnS10 (C). The bottom panel shows size distribution histograms of MnQDs from TEM data. The average diameters of Mn02ZnS10, Mn05ZnS10, and Mn17ZnS10 are 10.7, 10.3, and 11.1 nm, respectively.

milliseconds (see Tables 3 and 4 for fitting results and Supporting Information, Figures S11 and S12 for traces and fits), indicating the existence of BET from Mn^{2+}.

To quantify the ratiometric temperature sensitivity in DPA-MnQDs with different shell thicknesses, the exciton emission ratios (PL_{exc}/PL_{total}) at different temperatures were measured. As mentioned above, the PL_{exc}/PL_{total} ratio is obtained from the ratio of the integrated PL intensity between 415 and 565 nm to its total PL intensity. The temperature sensitivity of DPA-MnQDs is represented by the slope of PL_{exc}/PL_{total} as a function of temperature, shown in Figure 3D. They are $(2.6 \pm 0.3) \times 10^{-3}$, $(4.0 \pm 0.4) \times 10^{-3}$, and $(3.0 \pm 0.3) \times 10^{-3}$ °C^{-1} for DPA-Mn08ZnS02, DPA-Mn08ZnS05, and DPA-Mn08ZnS10, respectively.

The nonradiative relaxation rate of the excitonic state tends to increase at higher temperatures, resulting in reduced emission intensity. The contribution of the temperature-dependent nonradiative relaxation channel can be examined by plotting the total intensity PL_{total} as a function of temperature, shown in Figure 3E. It is evident that the DPA-Mn08ZnS02 construct exhibits significant temperature-dependent PL intensity reduction; therefore, the slope shown in Figure 3D for this construct is primarily driven by the reduction of the total intensity, rather than by the relative populations

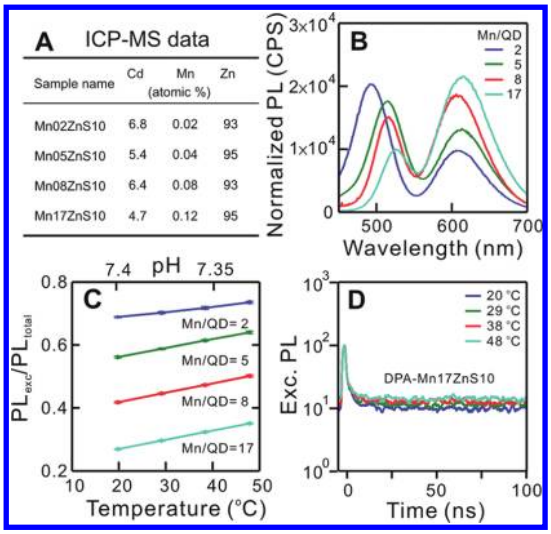

Figure 5. (A) ICP–MS data of MnQDs (*via* Route A). (B) PL spectra of DPA-MnQDs with different Mn^{2+} concentration (Mn/QD) in 1X PBS buffer solution. The PL spectra were normalized to the integrated intensity. (C) Temperature-dependent PL_{exc}/PL_{total} plots of DPA-MnQDs with different Mn^{2+} concentration in 1X PBS buffer solution. Top pH value axis was measured from blank 1X PBS at different temperatures. The error bars are one standard deviation from the average values collected from the heating–cooling cycling measurements (Supporting Information, Figure S6). (D) Normalized temperature-dependent exciton emission lifetime traces of DPA-Mn17ZnS10 in 1X PBS buffer solution. The lifetime traces were smoothed by averaging adjucent 17 data points and normalized to the intensity maximum.

of the Mn^{2+} and the excitonic states. This argument was supported by the lifetime trace of DPA-Mn08ZnS02 (Figure 3F), which does not show a temperature-dependent intensity plateau as expected from BET (quantitative values are tabulated in the Table 2). In other words, the major contribution of temperature-dependent PL_{exc}/PL_{total} in DPA-Mn08ZnS02 is from the temperature-dependent ratio of nonradiative transition of exciton and Mn^{2+} emission. Therefore, the apparent PL_{exc}/PL_{total} ratio is due to the combined effect of the temperature-dependent BET and nonradiative relaxation of exciton and Mn^{2+} emission. The DPA-Mn08ZnS05 construct shows the highest temperature sensitivity among the three studied (Figure 3D) with moderate temperature-dependent PL_{total} intensity decrease (Figure 3E), suggesting a combined effect of BET and nonradiative transitions. In the subsequent studies, the MnQDs with thick ZnS shell (ZnS = 10.4 MLs) are used to examine the effect of Mn^{2+} concentration because the total PL intensity is the least sensitive (only about 6%) to temperature changes (Figure 3E).

To investigate the effect of Mn^{2+} dopant content, we prepared a series of samples with the nominal number of Mn^{2+} ion per QD at 2, 5, 8, and 17, designated as DPA-Mn02ZnS10, DPA-Mn05ZnS10, DPA-Mn08ZnS10, and DPA-Mn17ZnS10, respectively. The TEM images and ICP–MS results of the MnQDs with different Mn/QD are shown in Figure 4 and 5A (additional structural

characterization results, EDS and XRD, are shown in Supporting Information, Figure S7). The Mn/QD dependent photoluminescence spectra of DPA-MnQDs at 20 °C are displayed in Figure 5B. With increasing Mn^{2+} concentration, the relative exciton emission intensity decreases, suggesting that the Mn^{2+} sites deplete energy from the excitonic state. The shifts in the Mn^{2+} emission peak position of DPA-MnQDs are likely caused by batch-to-batch variations. Following the earlier studies,[52−54] the red-shifts of exciton emission with increasing Mn^{2+} concentration can be attributed to the exchange interaction between the Mn^{2+} ion and the band electrons. The temperature-dependent PL_{exc}/PL_{total} for this series of DPA-MnQDs are displayed in Figure 5C, exhibiting slopes of $(1.7 \pm 0.3) \times 10^{-3}$, $(3.1 \pm 0.1) \times 10^{-3}$, $(3.0 \pm 0.3) \times 10^{-3}$, and $(3.0 \pm 0.1) \times 10^{-3}$ °C^{-1}, for Mn/QD = 2, 5, 8, and 17, respectively. The temperature sensitivity (slope) of DPA-Mn02ZnS10 appears to be significantly lower than that of other samples, likely due to fewer Mn^{2+} sites available for energy storage and consequently lowering the contribution from BET and possibly the contribution of undoped dot in the sample. Conversely, DPA-MnQDs with higher Mn^{2+} concentrations (5 Mn/QD and above) exhibit similar temperature sensitivities. This result suggests that high Mn^{2+} concentration is necessary for good temperature sensitivity. It also implies that potential dot-to-dot variations in Mn^{2+} concentration may be alleviated for temperature measurement applications with a larger Mn/QD ratio.

Insights about the relative excitonic populations due to BET from the Mn^{2+} dopant can be obtained from photoluminescence lifetime measurements. As before, the exciton decay lifetimes of DPA-MnQDs with lower Mn^{2+} concentrations (Mn/QD at 2, 5, 8) are similar (11−18 ns), shown in Table 2. Figure 5D displays temperature-dependent lifetime traces of DPA-Mn17ZnS10, where the plateau intensities are seen to increase with temperature, indicating a greater BET contribution with higher temperatures.

Assuming that the ∼10-ns exciton decay exclusively comes from undoped DPA-MnQDs, we developed a method to estimate the extent of undoped dots in our samples based on the lifetime traces (see the Methods section for details). The estimated amounts of undoped dots were 15%, 14%, 6.8%, and 3.4% for Mn/QD = 2, 5, 8, and 17, respectively. It should be pointed out that quencher-decorated quantum dots could exhibit excursions to high-emission and long-lifetime states on the single-particle level, as has been nicely demonstrated by Song *et al.*[55] Therefore, the estimation assuming the ∼10-ns component comes exclusively from undoped quantum dots is an upper bound for the percentage of undoped DPA-MnQDs. In addition, assuming the distribution of Mn^{2+} in the samples follows the Poisson statistics, the amount of undoped dots were estimated to be 14%, 0.67%, 0.03%, and 0% for Mn/QD = 2, 5, 8, and 17, respectively (Supporting Information, Figure S8A). This result is consistent with the PL spectrum of Mn17ZnS10 measured at low temperature (*ca.* −50 °C), where exciton emission was not observed (Figure S8B). Furthermore, the temperature sensitivities (slopes) of DPA-MnQDs with high Mn^{2+} concentration (Mn/QD ≥ 5) are almost the same, implying the contributions of undoped dots on temperature sensing in the DPA-MnQDs with high Mn^{2+} concentrations (Mn/QD ≥ 5) are negligible.

To further characterize the sensitivity of DPA-MnQDs, the precision of the temperature sensing, that is, the extent of temperature-dependent uncertainties, was estimated from the error bars in the temperature-dependent PL_{exc}/PL_{tot} plots, shown in Table 1. Low precision (∼2.2 °C) was obtained from the DPA-MnQDs with thin ZnS shell (DPA-Mn08ZnS02) and low Mn^{2+} dopant concentration (DPA-Mn02ZnS10). The precision of the DPA-MnQDs with thick ZnS shell and high Mn^{2+} dopant concentration was relatively high, ∼0.59 °C (in DPA-Mn05ZnS10), comparable to the precision of the previously reported MnQDs in toluene.[24] These results support that a thick ZnS shell and high Mn^{2+} dopant concentration are two key parameters to maintaining excellent temperature sensitivity in aqueous solutions.

CONCLUDING REMARKS

Quantum dot-based sensors, in principle, could provide information regarding the long-term evolution of nanoscale local environments in biological samples, for example, pH,[56,57] redox potential,[57−59] and most recently temperature.[20] The new pieces of information are expected to accelerate the pace of many research areas, particularly those that strive to achieve molecule-level understanding of biological systems.[60] Factors that have limited their wider-spread use include cost, availability, biocompatibility, sizes, toxicity, and emission intermittency.[61] To gain biologically relevant insights, moreover, the quantum dot probes usually have to be finely tuned. The optimization process may involve highly sophisticated procedures and equipment, requiring resources that are not available to most laboratories focused on biophysical and molecular cell biology. Our economical and accessible approach reported herein allows researchers to synthesize their own temperature-sensitive Mn^{2+}-doped quantum dots (MnQDs), eliminating two major limiting factors (cost and availability). Biocompatible temperature-sensitive MnQDs can be optimized for specific applications by modifying the inorganic surface of the QDs with appropriate surfactant passivation. Considering the possible variations in the synthesis and passivation of these water-soluble MnQDs, the accuracy and precision of their temperature-sensing capability should be optimized and characterized on the application-by-application basis.

The approachable synthetic route described herein allows this optimization process to be achieved. In addition to the synthesis of temperature-sensing MnQDs with a new base structure, our results also suggest that the idea of using the emission intensity ratio between two thermally coupled emissive states as originally proposed for rare-earth-doped materials for temperature sensing is generalizable, providing the foundation for further creative ways of measuring local temperature in complex environments.

METHODS

Materials. All chemicals were used without further purification. Diphenylphosphine (98%), manganese(II) acetate (98%), sulfur (99.998%), cadmium oxide (CdO, ≥ 99.99%), olelylamine (Tech grade), oleic acid (Tech 90%), anhydrous toluene (99.8%), and D-penicillamine (DPA, 98−101%) were purchased from Sigma-Aldrich. 1-Octadecene (ODE, 90% Tech) and cadmium acetate dehydrate (98%) were purchased from Acros organics. Selenium shots (99.999+%) and zinc stearate (cat. no. 33238) were purchased from Alfa Aesar.

Preparation of Diphenylphosphine Selinide (DPPSe). DPPSe was prepared by following previously published procedures.[62] A mixture of selenium shot (1.5 g, 20 mmol) and diphenylphosphine (3.48 mL, 20 mmol) was dissolved in 25 mL of anhydrous toluene in a three-neck flask under N_2 environment. The mixture was refluxed for 16 h, forming a clear and slightly yellow solution. Toluene was removed under reduced pressure, and the resulting white solid powder (DPPSe) was collected and stored. Note that diphenylphosphine (DPP) is a pyrophoric chemical. To perform the synthesis of DPPSe without using a glovebox, it is necessary to purchase DPP (252964-50G, Sigma-Aldrich) and anhydrous toluene (244511-100ML, Sigma-Aldrich) stored in septum-sealed bottles. DPP and anhydrous toluene were transferred using syringes into the flask containing selenium after proper degassing and subsequent placement in nitrogen environment at room temperature. After the reaction, the air-stable DPPSe is formed. A large quantity of DPPSe can be prepared, so the synthesis of DPPSe does not need to be performed very often.

Synthesis of CdSSe Nanocrystals Using DPPSe (Route A). The synthetic procedure was modified from a previously published procedure.[42] Colloidal CdSSe nanocrystals were prepared by injecting sulfur−selenium (S−Se) precursor into a hot cadmium (Cd) precursor solution. The S−Se stock solution (molar ratio 60:40) was freshly prepared using 38.4 mg of sulfur, 212 mg of DPPSe, and 8 mL of ODE in a three-neck 50-mL flask. (Aged S−Se stock solution may cause the first absorption and emission peaks of the CdSSe core to blue shift, indicating a decrease of Se content in the nanocrystals.) The solution was degassed, refilled with nitrogen and heated to 120 °C, producing a yellow solution. In a separate three-neck flask, a Cd precursor stock solution was prepared using 128 mg of CdO, 2.4 mL of oleic acid, and 8 mL of ODE. The solution was degassed, refilled with nitrogen, and heated to 280 °C, producing a clear solution. A 2 mL portion of S−Se stock solution was injected into the Cd precursor solution, lowering the temperature to 265 °C. After injection, the mixture turned orange, indicating the formation of CdSSe nanocrystals. The temperature was kept at 265 °C for about 8 min for further nanocrystal growth. The reaction was quenched by removing the heat source, and the resulting solution was cooled to room temperature. Unreacted precursors and excess surfactants were removed by performing the following washing procedure. The resulting nanocrystals were precipitated by adding acetone. A pellet of nanocrystals was formed after centrifugation at 4000 rpm for 10 min. The supernatant was discarded, and the yellow pellet containing CdSSe was resuspended in 10 mL of toluene. A 10 mL portion of methanol was added, forming a turbid solution, and the mixture was centrifuged at 4000 rpm for 5 min. The supernatant was discarded, and the yellow precipitate was resuspended in 7 mL of hexane. The nanocrystals were centrifuged again for 5 min at 4000 rpm to remove undesirable large particles, and the yellow transparent solution was filtered through a 0.2 μm polytetrafluoroethylene (PTFE) filter (Fisherbrand, 09-719G) into an amber vial. The resultant CdSSe cores were stored at 4 °C.

Synthesis of CdSSe Nanocrystals Using Se Powder (Route B). The nanocrystals were prepared according to previously published noninjection procedures with minor modifications.[63,64] For 40% Se nanocrystals, 1 mmol of cadmium acetate dihydrate, 15 mL of ODE and 2.4 mL of oleic acid were heated at 120 °C for 30 min under vacuum. The resulting clear solution was cooled under N_2 flow to 30 °C and added to a dry mixture of 0.2 mmol of Se and 0.3 mmol of S degassed in a three-neck round-bottom flask. The reaction mixture was raised to 240 °C under N_2 environment at a rate of 10 °C per minute. When the reaction reached 240 °C, the reaction time began. Nanocrystals were allowed to grow for 3 min after which the reaction was quenched by injecting 8 mL of ambient temperature ODE. The product was cooled to room temperature by removing the heat source. The washing step followed the same procedure described above.

Preparation of Zinc, Sulfur, and Manganese Precursor Solutions for Mn^{2+}-doped QDs. A 0.04 M zinc stearate ($Zn(St)_2$) stock solution was prepared using 1.01 g of $Zn(St)_2$, 1 mL of oleic acid, and 39 mL of ODE. The solution was degassed, refilled with nitrogen, and kept at room temperature. A 0.04 M sulfur stock solution was prepared using 51.2 mg of sulfur and 40 mL of ODE. The solution was degassed, refilled with nitrogen, and heated to 120 °C. The resulting clear solution was cooled to 60 °C. A 7.25 mM manganese (Mn) precursor solution was prepared using 10.4 mg of manganese(II) acetate. After the powder was degassed at room temperature for 10 min, 8 mL of oleylamine was injected into the flask. After an additional 10 min, the resulting clear, pale-yellow solution was refilled with nitrogen and kept at room temperature. The Mn precursor solution needs to be prepared immediately prior to use to avoid oxidation. Oxidation of Mn precursor can be easily observed by the color change from clear to brown.

Synthesis of Mn^{2+}-Doped QDs from CdSSe Cores. Mn^{2+}-doped QDs were prepared by following previously published procedures with minor modifications.[28,29] In the published procedures, Mn^{2+}-doped QDs were prepared by three separated steps—the initial ZnS shell coating, Mn cation doping, and the final ZnS shell coating. To simplify the synthetic procedure, the three separated steps were combined. First, CdSSe nanocrystal cores ($\sim 6 \times 10^{-8}$ mol) were placed in a three-neck flask with 2 mL of oleylamine and 6 mL of ODE. The mixture was degassed to remove hexane, refilled with nitrogen, and heated to 120 °C. The ZnS shell coating was performed following the SILAR procedure,[65] where approximately 0.8 monolayer (ML) of ZnS shell was grown in every cycle. A 0.52 mL portion of 0.04-M sulfur stock solution was added dropwise into the mixture and heated to 220 °C for 10 min. A 0.52 mL portion of 0.04-M $Zn(St)_2$ stock solution was added dropwise into the mixture, and kept at 220 °C for another 10 min, forming 0.8 ML of ZnS shell. Another 0.8 ML of ZnS was coated by dropwise addition of 0.64-mL sulfur stock solution and 0.64-mL $Zn(St)_2$ stock solution at 220 °C where each sulfur or Zn addition was metered over 10 min. After the mixture was heated to 280 °C, 0.90 mL of 0.04-M sulfur stock solution and 0.79 mL of 7.25-mM Mn stock solution were added dropwise, and the mixture was kept at 280 °C for 20 min. Note that the Mn-growth (measured/added) yield is ~11% according to the inductively coupled plasma mass spectroscopy (ICP−MS) data measured by Evans Analytical Group. A 0.79 mL portion of 0.04-M Zn stock solution was added at 280 °C, and the mixture was kept at 280 °C for 10 min. After the QD was doped with Mn, the subsequent ZnS shell coating was performed by growing 0.8 ML of ZnS sequentially at 280 °C until the desired thickness

of ZnS shell was obtained. The product was cooled down to room temperature by removing the heat source. The washing step followed the same procedure described for the CdSSe cores. Note that all the data described in the manuscript was collected from the MnQDs *via* Route A, and the temperature sensing data of the MnQDs *via* Route B is presented in the Supporting Information; 10.4 MLs of external ZnS layers of MnQDs were achieved by coating an additional 5.6 MLs of ZnS shell on the MnQDs with 4.8 MLs of ZnS shell after washing.

DPA Passivation Procedure. The DPA passivation procedure was modified based on previous procedures, primarily through the use of sonication to accelerate the passivation process.[31,45] Briefly, water-soluble passivation was conducted by sonicating 10 nmol of Mn^{2+}-doped QDs suspended in 400 μL of 0.8-M NaOH/methanol solution with D-penicillamine (100 mg/mL) and 900 μL of chloroform for 1 h. Biphasic exchange was performed by the addition of 0.1-mL 1X PBS and additional sonication for 20 min. To retrieve the water-soluble MnQDs, the top aqueous layer was collected, treated with ethanol, and then centrifuged at 4000 rpm for 10 min. The precipitated DPA-coated MnQDs (DPA-MnQDs) were then redispersed in 1× PBS (pH = 7.4) buffer. The DPA-MnQDs were annealed to provide better stability in water-based solvents for photoluminescence and lifetime measurements.

Photoluminescence Quantum Yield Measurements. The photoluminescence quantum yields of DPA-MnQDs were estimated from the integrated PL intensity ratio of DPA-MnQDs to a reference dye, quinine in 0.1-M H_2SO_4, the quantum yield of which is reported to be ~55%.[66] The measurements were performed at 20 °C, and the excitation wavelength was 350 nm with 1-nm excitation width.

Photoluminescence and Lifetime Measurements. Photoluminescence measurements were performed using the Fluorolog-3 fluorometer (Horiba Jobin-Yvon). Exciton lifetime measurements were performed using the time-correlated single photon counting (TCSPC) option of the fluorometer where the QDs were excited by a NanoLED device. The excitation wavelength was 445 nm with pulse duration of about 1.2 ns. The detection wavelength was set to the peak position of exciton emission with a spectral window of 10 nm. The fluorescence lifetime window was set to a time range of 200 ns. The PL lifetimes on microsecond and millisecond time scale were obtained using the multichannel scaler (MCS) option of the fluorometer where the MnQDs were excited by SpectraLED device (excitation wavelength was 390 nm). The detection wavelengths were set to 510 nm for exciton emission and 620 nm for Mn^{2+} emission with a spectral window of 15 nm. The lifetime window was set to a time range of 80 ms with a time resolution of 20 μs. The dark counts of PL lifetime traces on microsecond and millisecond time scale were subtracted before the performance of curve fitting. Additional PL lifetime data and fitting results were shown in the Supporting Information.

Analysis of Photoluminescence Lifetime. The nanosecond PL lifetime decays at the 510-nm exciton emission were fitted to a biexponential model,

$$g_{ns}(t) = N_{ns}\left[\frac{f_1}{\tau_1}e^{-t/\tau_1} + \frac{1-f_1}{\tau_2}e^{-t/\tau_2}\right]\delta t + B_{ns} + g_{offset} \quad (1)$$

where N_{ns} is the number of photons from the nanosecond decay channels, f_1 is the fraction of the faster decay channel ($\tau_1 < 1$ ns), δt is the TCSPC digitization time ($\delta t = 0.2237$ ns in the present case), B the background count of the fluorometer measured from a separate control experiment, and g_{offset} is the signal offset resulting from the back energy transfer from the coupling Mn^{2+} ions. Equation 1 was convolved with an instrument response function and compared with the PL lifetime. The optimal N_{ns}, f_1, τ_1, τ_2, and g_{offset} were located through a χ^2 minimization procedure.

The millisecond PL lifetime decays were fitted to a stretched exponential (Kohlrausch−Williams−Watts) model,

$$g_{ms}(t) = N_{ms}\frac{1}{\tau_{KWW}\Gamma[1+\beta_{KWW}^{-1}]}\exp\left[-\left(\frac{t}{\tau_{KWW}}\right)^{\beta_{KWW}}\right]\delta t + B_{ms} \equiv N_{ms}g_{KWW}(t) + B_{ms} \quad (2)$$

where N_{ms} is the number of photons from the millisecond decay channels, τ_{KWW} and β_{KWW} are parameters for the stretched exponential, δt the TCSPC digitization time (δt = 20 μs in the present case), and B_{ms} is the background. The parameters N_{ms}, τ_{KWW} and β_{KWW} were optimized through a χ^2 minimization procedure after convolving eq 2 with an instrument response function on this time scale. The expectation value for the millisecond lifetime was calculated using the optimized parameters with the formula

$$\langle\tau\rangle_{KWW} = \int_0^\infty \frac{t}{\tau_{KWW}\Gamma[1+\beta_{KWW}^{-1}]}\exp\left[-\left(\frac{t}{\tau_{KWW}}\right)^{\beta_{KWW}}\right]dt = \frac{\tau_{KWW}\Gamma[1+2\beta_{KWW}^{-1}]}{2\Gamma[1+\beta_{KWW}^{-1}]}$$

Error bars for the PL decay parameters were calculated using the analytical covariance matrices derived from eqs 1 and 2.[67] Unless specified, all data analyses were carried out using Matlab (Mathworks, version 2011a).

Estimation of Undoped MnQD Percentage. The probability for a photon from the millisecond-decay channel to appear in the nanosecond window is expected to be diminishingly small. However, if the relative population through the millisecond channel is great, as in the present case, it will become detectable in the nanosecond time window. That is, the approximate millisecond decay from the BET contribution to the exciton radiative relaxation on the nanosecond time window would appear as a constant offset, denoted as g_{offset} in eq 1. Once the parameters of the millisecond decay were determined, *cf.*, eq 2, the probability for one photon from the millisecond channel to appear in the nanosecond window can be calculated by $g_{ns\leftarrow ms} \approx \sum_{k=0}^{\infty} g_{KWW}(kT)$, where T is the period between consecutive laser excitation pulses. The summation takes into account the situation when the stop signal (the laser pulse immediately following the excitation pulse) arrives before the millisecond PL decay has completed in a TCSPC setup. In the present case, T = 1 μs for the nanosecond PL lifetime measurements and the summation was calculated numerically. At the exciton emission wavelength, the number of photons coming from undoped and doped MnQDs are $N_{undoped} = N_{ns}(1 - f_1)$ and $N_{doped} = g_{offset}/g_{ns\leftarrow ms}$, respectively. The percentage of undoped MnQDs in a sample is therefore, $P_{undoped} = N_{undoped}/(N_{undoped} + N_{doped})$.

Temperature-Dependent Photoluminescence Measurements. The excitation wavelength was set to 400 nm with 1-nm excitation width. The temperature-dependent measurements were conducted using a cuvette holder to hold the sample while water was pumped around the holder from an external circulating temperature bath. The temperature was measured by inserting a thermocouple probe through a septum-capped cuvette. The temperature-dependent PL spectra were collected from DPA-MnQDs in PBS buffer solution.

Transmission Electron Microscopy. TEM images were collected using the Philips CM100 TEM. The sample was prepared by adding a drop of diluted MnQDs in hexane solution on a carbon-supported copper grid. The TEM images were analyzed using the image processing toolbox in the Matlab. The TEM images were converted into black-and-white images. To ensure the black and white images well present the nanocrystals in the original TEM images, it is necessary to fine-tune the threshold for the image conversion. In the black and white binary image, the connected pixels were considered as nanocrystals. The diameters of nanocrystals were estimated from the area of the connected components, assuming all the particles are circular on a two-dimensional projection of TEM. In general, the average diameters were obtained from more than 500 particles, which are consistent with the hand-measured values (100 particles).

Acknowledgment. This work was supported by Princeton University, and in part by the U.S. Department of Energy. We thank E. Yates and M. Sampias for the initial development of the DPA passivation procedure. We thank the Imaging and Analysis Center of Princeton University for assisting with TEM, XRD, and EDS measurements.

Supporting Information Available: Temperature-dependent PL spectra of Mn^{2+}-doped (CdS)ZnS quantum dots (Figure S1), Mn^{2+}-doped (CdSe)ZnCdS quantum dots (Figure S4), and Mn^{2+}-doped (CdSSe)ZnS quantum dots *via* Route B (Figure S3); absorption and PL spectra of CdSSe cores (Figure S2); TEM image of Mn^{2+}-doped (CdSe)ZnS (Figure S4); PL spectra of MnQDs prepared at different reaction temperatures *via* Route A (Figure S5); temperature dependent cycles of PL_{exc}/PL_{total} of DPA-Mn17ZnS10 in 1X PBS (Figure S6); additional structural characterization data (Figure S3 and S7); Mn^{2+} dopant concentration distribution of the MnQDs estimated using the Poisson statistics (Figure S8A); low temperature PL spectrum of Mn17ZnS10 (Figure S8B); additional PL lifetime data and fits (Figure S9–S12); temperature dependent PL_{exc}/PL_{total} plots of the MnQDs in a wide temperature range (Figure S13). This material is available free of charge *via* the Internet at http://pubs.acs.org.

REFERENCES AND NOTES

1. Mergny, J.-L.; Lacroix, L. Analysis of Thermal Melting Curves. *Oligonucleotides* **2003**, *13*, 515–537.
2. Narberhaus, F.; Waldminghaus, T.; Chowdhury, S. RNA Thermometers. *FEMS Microbiol. Rev.* **2006**, *30*, 3–16.
3. Sanchez-Ruiz, J. M. Protein Kinetic Stability. *Biophys. Chem.* **2010**, *148*, 1–15.
4. Walker, G. W.; Sundar, V. C.; Rudzinski, C. M.; Wun, A. W.; Bawendi, M. G.; Nocera, D. G. Quantum-Dot Optical Temperature Probes. *Appl. Phys. Lett.* **2003**, *83*, 3555–3557.
5. Uchiyama, S.; Matsumura, Y.; de Silva, A. P.; Iwai, K. Fluorescent Molecular Thermometers Based on Polymers Showing Temperature-Induced Phase Transitions and Labeled with Polarity-Responsive Benzofurazans. *Anal. Chem.* **2003**, *75*, 5926–5935.
6. Lee, J.; Govorov, A. O.; Kotov, N. A. Nanoparticle Assemblies with Molecular Springs: A Nanoscale Thermometer. *Angew. Chem.* **2005**, *117*, 7605–7608.
7. Kusama, H.; Sovers, O. J.; Yoshioka, T. Line Shift Method for Phosphor Temperature Measurements. *Jpn. J. Appl. Phys.* **1976**, *15*, 2349–2368.
8. Berthou, H.; Jörgensen, C. K. Optical-Fiber Temperature Sensor Based on Upconversion-Excited Fluorescence. *Opt. Lett.* **1990**, *15*, 1100–1102.
9. Ross, D.; Gaitan, M.; Locascio, L. E. Temperature Measurement in Microfluidic Systems Using a Temperature-Dependent Fluorescent Dye. *Anal. Chem.* **2001**, *73*, 4117–4123.
10. Resch-Genger, U.; Grabolle, M.; Cavaliere-Jaricot, S.; Nitschke, R.; Nann, T. Quantum Dots *versus* Organic Dyes as Fluorescent Labels. *Nat. Methods* **2008**, *5*, 763–775.
11. Li, S.; Zhang, K.; Yang, J.-M.; Lin, L.; Yang, H. Single Quantum Dots as Local Temperature Markers. *Nano Lett.* **2007**, *7*, 3102–3105.
12. Joshi, A.; Narsingi, K. Y.; Manasreh, M. O.; Davis, E. A.; Weaver, B. D. Temperature Dependence of the Band Gap of Colloidal CdSe/ZnS Core/Shell Nanocrystals Embedded into an Ultraviolet Curable Resin. *Appl. Phys. Lett.* **2006**, *89*, 131907.
13. Valerini, D.; Cretí, A.; Lomascolo, M.; Manna, L.; Cingolani, R.; Anni, M. Temperature Dependence of the Photoluminescence Properties of Colloidal CdSe/ZnS Core/Shell Quantum Dots Embedded in a Polystyrene Matrix. *Phys. Rev. B* **2005**, *71*, 235409.
14. Rudin, S.; Reinecke, T. L.; Segall, B. Temperature-Dependent Exciton Linewidths in Semiconductors. *Phys. Rev. B* **1990**, *42*, 11218.
15. Hwang, Y.-N.; Park, S.-H.; Kim, D. Size-Dependent Surface Phonon Mode of CdSe Quantum Dots. *Phys. Rev. B* **1999**, *59*, 7285.
16. Zheng, J. P.; Kwok, H. S. Temperature Dependence of the Optical Properties of Semiconductor Microcrystals. *J. Opt. Soc. Am. B* **1992**, *9*, 2047–2053.
17. Gindele, F.; Hild, K.; Langbein, W.; Woggon, U. Temperature-Dependent Line Widths of Single Excitons and Biexcitons. *J. Lumin.* **2000**, *87–89*, 381–383.
18. Yang, J.-M.; Yang, H.; Lin, L. Thermogenesis Detection of Single Living Cells *via* Quantum Dots. In *The 23rd IEEE Micro Electro Mechanical Systems Conference*; IEEE: Hong Kong, 2010; pp 963–966.
19. Maestro, L. M.; Rodríguez, E. M.; Sanz-Rodríguez, F.; Iglesias-de la Cruz, M. C.; Juarranz, A.; Naccache, R.; Vetrone, F.; Jaque, D.; Capobianco, J. A.; Solé, J. G. CdSe Quantum Dots for Two-Photon Fluorescence Thermal Imaging. *Nano Lett.* **2010**, *10*, 5109–5115.
20. Yang, J.-M.; Yang, H.; Lin, L. Quantum Dot Nanothermometers Reveal Heterogeneous Local Thermogenesis in Living Cells. *ACS Nano* **2011**, *5*, 5067–5071.
21. Vetrone, F.; Naccache, R.; Zamarrón, A.; Juarranz de la Fuente, A.; Sanz-Rodríguez, F.; Martinez Maestro, L.; Martín Rodriguez, E.; Jaque, D.; García Solé, J.; Capobianco, J. A. Temperature Sensing Using Fluorescent Nanothermometers. *ACS Nano* **2010**, *4*, 3254–3258.
22. Ye, F.; Wu, C.; Jin, Y.; Chan, Y.-H.; Zhang, X.; Chiu, D. T. Ratiometric Temperature Sensing with Semiconducting Polymer Dots. *J. Am. Chem. Soc.* **2011**, *133*, 8146–8149.
23. Wade, S. A.; Collins, S. F.; Baxter, G. W. Fluorescence Intensity Ratio Technique for Optical Fiber Point Temperature Sensing. *J. Appl. Phys.* **2003**, *94*, 4743–4756.
24. Vlaskin, V. A.; Janssen, N.; van Rijssel, J.; Beaulac, R.; Gamelin, D. R. Tunable Dual Emission in Doped Semiconductor Nanocrystals. *Nano Lett.* **2010**, *10*, 3670–3674.
25. A similar idea for water-soluble temperature-sensing quantum dots was reported in a recently accepted manuscript by McLaurin, Vlaskin, Gamelin, J. Am. Chem. Soc. (**2011**), which was submitted two weeks after the submission of this manuscript to *ACS Nano*.
26. The definition of "Green Chemistry" can be found on the U. S. Environmental Protection Agency web site, http://www.epa.gov/gcc/.
27. Peng, Z. A.; Peng, X. Formation of High-Quality CdTe, CdSe, and CdS Nanocrystals Using CdO as Precursor. *J. Am. Chem. Soc.* **2000**, *123*, 183–184.
28. Yang, Y.; Chen, O.; Angerhofer, A.; Cao, Y. C. Radial-Position-Controlled Doping in CdS/ZnS Core/Shell Nanocrystals. *J. Am. Chem. Soc.* **2006**, *128*, 12428–12429.
29. Yang, Y.; Chen, O.; Angerhofer, A.; Cao, Y. C. On Doping CdS/ZnS Core/Shell Nanocrystals with Mn. *J. Am. Chem. Soc.* **2008**, *130*, 15649–15661.
30. Susumu, K.; Oh, E.; Delehanty, J. B.; Blanco-Canosa, J. B.; Johnson, B. J.; Jain, V.; Hervey, W. J.; Algar, W. R.; Boeneman, K.; Dawson, P. E.; *et al.* Multifunctional Compact Zwitterionic Ligands for Preparing Robust Biocompatible Semiconductor Quantum Dots and Gold Nanoparticles. *J. Am. Chem. Soc.* **2011**, *133*, 9480–9496.
31. Breus, V. V.; Heyes, C. D.; Tron, K.; Nienhaus, G. U. Zwitterionic Biocompatible Quantum Dots for Wide pH Stability and Weak Nonspecific Binding to Cells. *ACS Nano* **2009**, *3*, 2573–2580.
32. Medintz, I. L.; Uyeda, H. T.; Goldman, E. R.; Mattoussi, H. Quantum Dot Bioconjugates for Imaging, Labelling and Sensing. *Nat. Mater.* **2005**, *4*, 435–446.
33. Murray, C. B.; Norris, D. J.; Bawendi, M. G. Synthesis and Characterization of Nearly Monodisperse CdE (E = S, Se, Te) Semiconductor Nanocrystallites. *J. Am. Chem. Soc.* **1993**, *115*, 8706–8715.
34. Bailey, R. E.; Nie, S. Alloyed Semiconductor Quantum Dots: Tuning the Optical Properties without Changing the Particle Size. *J. Am. Chem. Soc.* **2003**, *125*, 7100–7106.
35. Zhong, X.; Han, M.; Dong, Z.; White, T. J.; Knoll, W. Composition-Tunable $Zn_xCd_{1-x}Se$ Nanocrystals with High Luminescence and Stability. *J. Am. Chem. Soc.* **2003**, *125*, 8589–8594.
36. Schlegel, G.; Bohnenberger, J.; Potapova, I.; Mews, A. Fluorescence Decay Time of Single Semiconductor Nanocrystals. *Phys. Rev. Lett.* **2002**, *88*, 137401.
37. Zhang, K.; Chang, H.; Fu, A.; Alivisatos, A. P.; Yang, H. Continuous Distribution of Emission States from Single CdSe/ZnS Quantum Dots. *Nano Lett.* **2006**, *6*, 843–847.

38. Beaulac, R.; Archer, P. I.; van Rijssel, J.; Meijerink, A.; Gamelin, D. R. Exciton Storage by Mn^{2+} in Colloidal Mn^{2+}-Doped CdSe Quantum Dots. *Nano Lett.* **2008**, *8*, 2949–2953.
39. Fu, Y.; Agren, H.; Kowalewski, J. M.; Brismar, H.; Wu, J.; Yue, Y.; Dai, N.; Thylen, L. Radiative and Nonradiative Recombination of Photoexcited Excitons in Multishell-Coated CdSe/CdS/ZnS Quantum Dots. *EPL* **2009**, *86*, 37003.
40. Crooker, S. A.; Barrick, T.; Hollingsworth, J. A.; Klimov, V. I. Multiple Temperature Regimes of Radiative Decay in CdSe Nanocrystal Quantum Dots: Intrinsic Limits to the Dark-Exciton Lifetime. *Appl. Phys. Lett.* **2003**, *82*, 2793–2795.
41. Bol, A. A.; Meijerink, A. Long-Lived Mn^{2+} Emission in Nanocrystalline ZnS:Mn^{2+}. *Phys. Rev. B* **1998**, *58*, 15997–16000.
42. Chen, H.-Y.; Chen, T.-Y.; Son, D. H. Measurement of Energy Transfer Time in Colloidal Mn-Doped Semiconductor Nanocrystals. *J. Phys. Chem. C* **2010**, *114*, 4418–4423.
43. Michalet, X.; Pinaud, F. F.; Bentolila, L. A.; Tsay, J. M.; Doose, S.; Li, J. J.; Sundaresan, G.; Wu, A. M.; Gambhir, S. S.; Weiss, S. Quantum Dots for Live Cells, *in Vivo* Imaging, and Diagnostics. *Science* **2005**, *307*, 538–544.
44. Smith, A. M.; Duan, H.; Mohs, A. M.; Nie, S. Bioconjugated Quantum Dots for *in Vivo* Molecular and Cellular Imaging. *Adv. Drug Delivery Rev.* **2008**, *60*, 1226–1240.
45. Moloney, M. P.; Gun'ko, Y. K.; Kelly, J. M. Chiral Highly Luminescent CdS Quantum Dots. *Chem. Commun.* **2007**, 3900–3902.
46. Pradhan, N.; Battaglia, D. M.; Liu, Y.; Peng, X. Efficient, Stable, Small, and Water-Soluble Doped ZnSe Nanocrystal Emitters as Non-cadmium Biomedical Labels. *Nano Lett.* **2007**, *7*, 312–317.
47. Dabbousi, B. O.; Rodriguez-Viejo, J.; Mikulec, F. V.; Heine, J. R.; Mattoussi, H.; Ober, R.; Jensen, K. F.; Bawendi, M. G. (CdSe)ZnS Core−Shell Quantum Dots: Synthesis and Characterization of a Size Series of Highly Luminescent Nanocrystallites. *J. Phys. Chem. B* **1997**, *101*, 9463–9475.
48. Hines, M. A.; Guyot-Sionnest, P. Synthesis and Characterization of Strongly Luminescing ZnS-Capped CdSe Nanocrystals. *J. Phys. Chem.* **1996**, *100*, 468–471.
49. Kortan, A. R.; Hull, R.; Opila, R. L.; Bawendi, M. G.; Steigerwald, M. L.; Carroll, P. J.; Brus, L. E. Nucleation and Growth of Cadmium Selendie on Zinc Sulfide Quantum Crystallite Seeds, and *vice versa*, in Inverse Micelle Media. *J. Am. Chem. Soc.* **1990**, *112*, 1327–1332.
50. Ithurria, S.; Guyot-Sionnest, P.; Mahler, B.; Dubertret, B. Mn^{2+} as a Radial Pressure Gauge in Colloidal Core/Shell Nanocrystals. *Phys. Rev. Lett.* **2007**, *99*, 265501.
51. Chen, W.; Sammynaiken, R.; Huang, Y.; Malm, J.-O.; Wallenberg, R.; Bovin, J.-O.; Zwiller, V.; Kotov, N. A. Crystal Field, Phonon Coupling and Emission Shift of Mn^{2+} in ZnS:Mn Nanoparticles. *J. Appl. Phys.* **2001**, *89*, 1120–1129.
52. Giriat, W.; Stankiewicz, J. Photoluminescence in $Mn_xCd_{1-x}Se$ Crystals. *Phys. Status Solidi A-Appl. Res.* **1980**, *59*, K79–K80.
53. Lee, Y. R.; Ramdas, A. K.; Aggarwal, R. L. Energy Gap, Excitonic, and "Internal" Mn^{2+} Optical Transition in Mn-Based II−VI Diluted Magnetic Semiconductors. *Phys. Rev. B* **1988**, *38*, 10600.
54. Levy, L.; Hochepied, J. F.; Pileni, M. P. Control of the Size and Composition of Three Dimensionally Diluted Magnetic Semiconductor Clusters. *J. Phys. Chem.* **1996**, *100*, 18322–18326.
55. Song, N. S., N. H.; Zhu, H. M.; Jin, S. Y.; Zhan, W.; Lian, T. Q. Poisson-Distributed Electron-Transfer Dynamics from Single Quantum Dots to C60 Molecules. *ACS Nano* **2011**, *5*, 613–621.
56. Snee, P. T.; Somers, R. C.; Nair, G.; Zimmer, J. P.; Bawendi, M. G.; Nocera, D. G. A Ratiometric CdSe/ZnS Nanocrystal pH Sensor. *J. Am. Chem. Soc.* **2006**, *128*, 13320–13321.
57. Medintz, I. L.; Stewart, M. H.; Trammell, S. A.; Susumu, K.; Delehanty, J. B.; Mei, B. C.; Melinger, J. S.; Blanco-Canosa, J. B.; Dawson, P. E.; Mattoussi, H. Quantum-Dot/Dopamine Bioconjugates Function as Redox Coupled Assemblies for *in Vitro* and Intracellular pH Sensing. *Nat. Mater.* **2010**, *9*, 676–684.
58. Clarke, S. J.; Hollmann, C. A.; Zhang, Z.; Suffern, D.; Bradforth, S. E.; Dimitrijevic, N. M.; Minarik, W. G.; Nadeau, J. L. Photophysics of Dopamine-Modified Quantum Dots and Effects on Biological Systems. *Nat. Mater.* **2006**, *5*, 409–417.
59. Gutscher, M.; Pauleau, A.-L.; Marty, L.; Brach, T.; Wabnitz, G. H.; Samstag, Y.; Meyer, A. J.; Dick, T. P. Real-Time Imaging of the Intracellular Glutathione Redox Potential. *Nat. Method* **2008**, *5*, 553–559.
60. Yang, H. Progress in Single-Molecule Spectroscopy in Cells. *Curr. Opin. Chem. Biol.* **2010**, *14*, 3–9.
61. Klostranec, J. M.; Chan, W. C. W. Quantum Dots in Biological and Biomedical Research: Recent Progress and Present Challenges. *Adv. Mater.* **2006**, *18*, 1953–1964.
62. Evans, C. M.; Evans, M. E.; Krauss, T. D. Mysteries of TOPSe Revealed: Insights into Quantum Dot Nucleation. *J. Am. Chem. Soc.* **2010**, *132*, 10973–10975.
63. Zou, Y.; Li, D.; Yang, D. Noninjection Synthesis of CdS and Alloyed CdS_xSe_{1-x} Nanocrystals without Nucleation Initiators. *Nanoscale Res. Lett.* **2010**, *5*, 966–971.
64. Ouyang, J.; Vincent, M.; Kingston, D.; Descours, P.; Boivineau, T.; Zaman, M. B.; Wu, X.; Yu, K. Noninjection, One-Pot Synthesis of Photoluminescent Colloidal Homogeneously Alloyed CdSeS Quantum Dots. *J. Phys. Chem. C* **2009**, *113*, 5193–5200.
65. Li, J. J.; Wang, Y. A.; Guo, W. Z.; Keay, J. C.; Mishima, T. D.; Johnson, M. B.; Peng, X. G. Large-Scale Synthesis of Nearly Monodisperse CdSe/CdS Core/Shell Nanocrystals Using Air-Stable Reagents *via* Successive Ion Layer Adsorption and Reaction. *J. Am. Chem. Soc.* **2003**, *125*, 12567–12575.
66. Melhuish, W. H. Quantum Efficiencies of Fluoresence of Organic Substance—Effect of Solvent and Concentration of Fluorescent Solute. *J. Phys. Chem.* **1961**, *65*, 229–235.
67. Press, W. H.; Teukolsky, S. A.; Vetterling, W. T.; Flannery, B. P. *Numerical Recipes in C++: The Art of Scientific Computing*, 2 ed.; Cambridge University Press: Cambridge, U.K., 2002.